

Amorphous Iron(III)-Borate Nanolattices as Multifunctional Electrodes for Self-Driven Overall Water Splitting and Rechargeable Zinc–Air Battery

Weinan Zhao, Tao Xu, Tao Li, Yuankun Wang, Hui Liu, Jianze Feng, Shujiang Ding, Zhongtao Li,* and Mingbo Wu*

Highly stable and low-cost electrocatalysts with multi-electrocatalytic activities are in high demand for developing advanced energy conversion devices. Herein, a unique trifunctional amorphous iron-borate electrode is developed, which is capable of boosting hydrogen evolution, oxygen evolution, and oxygen reduction reactions simultaneously. The amorphous iron borate can self-assemble into well-defined nanolattices on electrode surface through a facile hydrothermal process, which possess more active sites and charge transfer pathways. As a result, the asymmetry overall water-splitting cell that adopts the amorphous electrodes as anode and cathode can be driven at 1.56 V with the current density of 10 mA cm⁻², which is lowest in state-of-the-art catalysts. Moreover, the water-splitting devices can be powered by a two-series-connected amorphous electrode-based zinc–air battery with high stability and Faradic efficiency (96.3%). The result can offer a potential and promising alternative way to develop metal-borate electrode for multifunctional applications.

1. Introduction

Developing renewable “hydrogenic energy” electrochemical devices such as water splitting, fuel cells, and metal–air batteries that were consisted with “half-reactions” of hydrogen evolution reaction (HER), oxygen evolution reaction (OER), and oxygen reduction reaction (ORR) would provide an efficient

way in addressing sustainability and energy crisis.^[1–3] Although some high active noble-metal-based catalysts have been developed, such as Pt/C for HER and ORR, and RuO₂ or IrO₂ for OER, these materials are still far from large-scale application due to the high cost and scarcity on earth.^[4,5] Therefore, great efforts have been made to solve these issues by developing cost-effective, earth-abundant catalysts for ORR, HER, and OER.^[6] Some electrocatalysts with transition metals have attracted more attentions due to the great electrochemical performance, such as metal–N–C for ORR,^[7] metal carbides/nitride^[8,9] and metal phosphides for HER; and metal hydroxides or metal carbonate for OER.^[10,11] However, integrating three functions (HER, OER, and ORR) into one catalysis is highly required to lower the cost and to extend applications, which

still meet great challenge due to the sluggish kinetics of varied multiple electron-transfer processes. So, it is important to deliberately modulate electrocatalysts' structure and morphology to achieve multifunctional applications and understand the relationship between catalytic activity and structure.^[12,13]

In general, the OER was more kinetically determining the two half-reactions, which leads to the majority increases of the activation overpotential during water splitting.^[14,15] Recently, a few reports demonstrated metal borates (M–Bi) exhibit advanced OER catalytic activity, which is attributed to the large negative charge of borate groups and modified electronic structures to bestow a low entropic energy during electrochemical processes,^[16] such as iron–cobalt-borate coating on carbon paper afforded 466 mV for OER for a current density of 10 mA cm⁻²,^[17] CoFe–LDH@CoFe–Bi on Ti mesh required an overpotential of 418 mV to achieve 10 mA cm⁻².^[18] Meanwhile, previous works also demonstrate the high ORR activity of some transition metal-based electrocatalysts (e.g., Fe, Co, and Ni) due to their unique 3d orbit.^[19,20] In this regard, explosion of novel transition metal borates to developing multifunctional catalysis was reasonable, where transition metal and borate would bring synergistic effects to optimize reactions.^[21] Moreover, it has been demonstrated that amorphous structure possessed higher density of active sites than those in crystalline state due to their short-range ordering and relatively crumby

W. Zhao, T. Xu, Dr. H. Liu, J. Feng, Dr. Z. Li, Prof. M. Wu
State Key Laboratory of Heavy Oil Processing
College of Chemical Engineering
University of Petroleum (East China)
Qingdao 266580, China
E-mail: liztao@upc.edu.cn; wumb@upc.edu.cn

T. Li
Yankuang National Engineering Research Center
of Coal Slurry Gasification and Coal Chemical Industry Co
Zaozhuang 277500, China

Dr. Y. Wang, Prof. S. Ding
Xi'an Key Laboratory of Sustainable Energy Materials Chemistry
School of Science
Xi'an Jiaotong University
Xi'an 710049, China

 The ORCID identification number(s) for the author(s) of this article can be found under <https://doi.org/10.1002/smll.201802829>.

DOI: 10.1002/smll.201802829

structure.^[22] Controllable integration of active amorphous substructures into catalyst and investigating its influence on electrocatalytic activity would offer a new avenue to improve the electrochemical performance, although these have been rarely reported so far.^[23]

Bearing this in mind, for the first time, an amorphous electrode with ferric borate (Fe–Bi) nanolattice on the surface of nickel foam (NF) has been exploited here, which possessed multiple catalysts in electrocatalysis. The amorphous Fe–Bi (am-Fe–Bi) was self-assembled into well-ordered nanolattices and cross-linked with each other on nickel foam, which could increase the specific surface area and afford more exposed active sites. Notably, the am-Fe–Bi on NF showed superior OER activity, which only affords 158 mV overpotential with the current density of 10 mA cm⁻². In addition, the amorphous Fe–Bi catalyst also possessed high HER (overpotential of 143 mV at 10 mA cm⁻²) and ORR activity (close to Pt/C, surpass RuO₂). The multifunction and high activity of the amorphous M–Bi electrode are first time reported to our knowledge. The significantly enhanced performance should be ascribed to the intrinsic competence (with suitable values of d-band center of catalysts and lower Gibbs energy during electrocatalysis) and structure control (amorphous nanolattices exposed more active sites). Finally, the am-Fe–Bi/NF electrodes are assembled into self-powered water splitting and two-series-connected zinc–air batteries, which could stably and effectively produce O₂ and H₂ (96.3% Faradic efficiency (FE)).

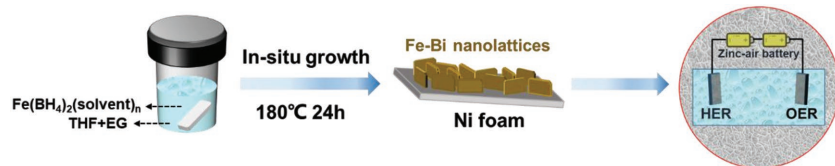
2. Result and Discussion

The amorphous electrode am-Fe–Bi/NF was prepared through the following facile solvent thermal method in **Scheme 1**. First, anhydrous ferric chloride and sodium borohydride were dissolved into the mixture of tetrahydrofuran (THF) and ethylene glycol (EG) solvents to make the homogeneous solution. A certain amount of methenamine was added to the mixture, which was sealed in a pressure vessel and reacted at an elevated temperature. As a control sample, the hydrothermal product, namely FeOOH/NF, is prepared through the same process except the introduction of sodium borohydride in the first step. The cr-Fe–Bi (cr-Fe–Bi/NF) was prepared through calcined am-Fe–Bi (am-Fe–Bi/NF) at 650 °C with N₂ protection.

As shown in **Figure 1a**, the X-ray photoelectron spectroscopy (XPS) peaks at 725.7 and 712 eV were ascribed to Fe 2p_{1/2} and 2p_{3/2}, respectively, which indicated the valence state of Fe⁺³.^[24] Meanwhile, the Fe 2p_{3/2} shows a higher binding energy in am-Fe–Bi/NF than that of 711.2 eV in FeOOH/NF, which indicates the higher oxidation state of Fe through the introduction of electronic negative borate (Figure S1, Supporting

Information).^[25] The binding energy of 191.7 eV in B 1s spectrum belongs to the B–O bonding in borate (Figure 1b). The O peaks could deconvolute into two major peaks at 530.9 and 531.6 eV, corresponding to the Fe–O–Fe and Fe–O–B bond in Fe–Bi, respectively (Figure 1c).^[26,27] In addition, the high contents of Fe–O–B in cr-Fe–Bi demonstrated the higher thermal stability of Fe–O–B than that of Fe–O–Fe. The characteristic of the Fourier transform infrared spectroscopy (FT-IR) (Figure 1d) further verified the existence of borate groups in both am-Fe–Bi/NF and cr-Fe–Bi (asymmetrical stretching vibration in borate and B–O stretching vibration at positions of 1379–1415, 883, and 1140 cm⁻¹, respectively).^[28] Figure S2 (Supporting Information) shows the X-ray powder diffraction (XRD) profile of am-Fe–Bi/NF, cr-Fe–Bi/NF, and FeOOH/NF, while am-Fe–Bi/NF shows no obvious crystalline diffraction peaks except metal Ni from substrate. After annealing at 650 °C, typical crystalline ferric borate diffraction peaks at 25.4° and 33.3° were obtained, which can be indexed to the (0 1 2) and (1 0 4) planes of ferric borate, respectively. To avoid the influence of Ni foam, we prepared the ferric borate (Fe–Bi) through the same procedure as cr-Fe–Bi except the addition of Ni foam. In Figure 1e, the experimental XRD patterns of Fe–Bi match well with standard iron-borate pattern (JCPDS No. 76-0701, 89-5642). All above data indicated the successful synthesis of amorphous Fe–Bi coating in the sample am-Fe–Bi/NF. As the control sample, the diffraction peaks of FeOOH and FeOOH/NF in Figure S3a (Supporting Information) indicated the presence of crystalline FeOOH (JCPDS No.44-1415) with a lattice fringe spacing of 0.283 nm (Figure S4a,b, Supporting Information).

As shown in Figure 1f and Figure S5 (Supporting Information), the morphologies of am-Fe–Bi/NF were investigated by a scanning electron microscope (SEM). Well-ordered lattices that consisted of cross-linked amorphous Fe–Bi nanosheets (among 15–20 nm thick) were uniformly distributed on Ni foam. Meanwhile, no diffraction lattice spacing inside the nanosheets could be identified in the high-resolution transmission electron microscopy (TEM) image (Figure 1g; Figure S6, Supporting Information), which would ascribe to an amorphous structure. Moreover, the amorphous structure could also be proved by the deficiency of fringe lattices in fast Fourier transformation (FFT, inset of Figure 1g). The energy dispersive X-ray spectroscopy (EDS) mapping (Figure 1h,i) indicated that Fe, Ni, O, and B were uniformly distributed in am-Fe–Bi/NF with no apparent aggregations. The coordination interactions with Fe and steric effect of borohydride groups seem to play an essential role on interrupting crystal growth during hydrothermal deposition. After annealing at 650 °C, the SEM images of cr-Fe–Bi/NF in Figure S7 (Supporting Information) show the cross-linked nanolattice, which has been broken into pieces. These nanosheets cross-staked with each other and the orientation became random after high-temperature calcination. Without introduction of sodium borohydride during the hydrothermal process, large amounts of nanocrystals were dispersed on the surface of FeOOH/NF as shown in Figure S8a–c (Supporting Information). The introduction of BH₄⁻ could form the more stable intermediate complex (Fe(BH₄)₂(solvent)_n) with Fe ion through



Scheme 1. Illustration of preparation of am-Fe–Bi/NF nanolattices.

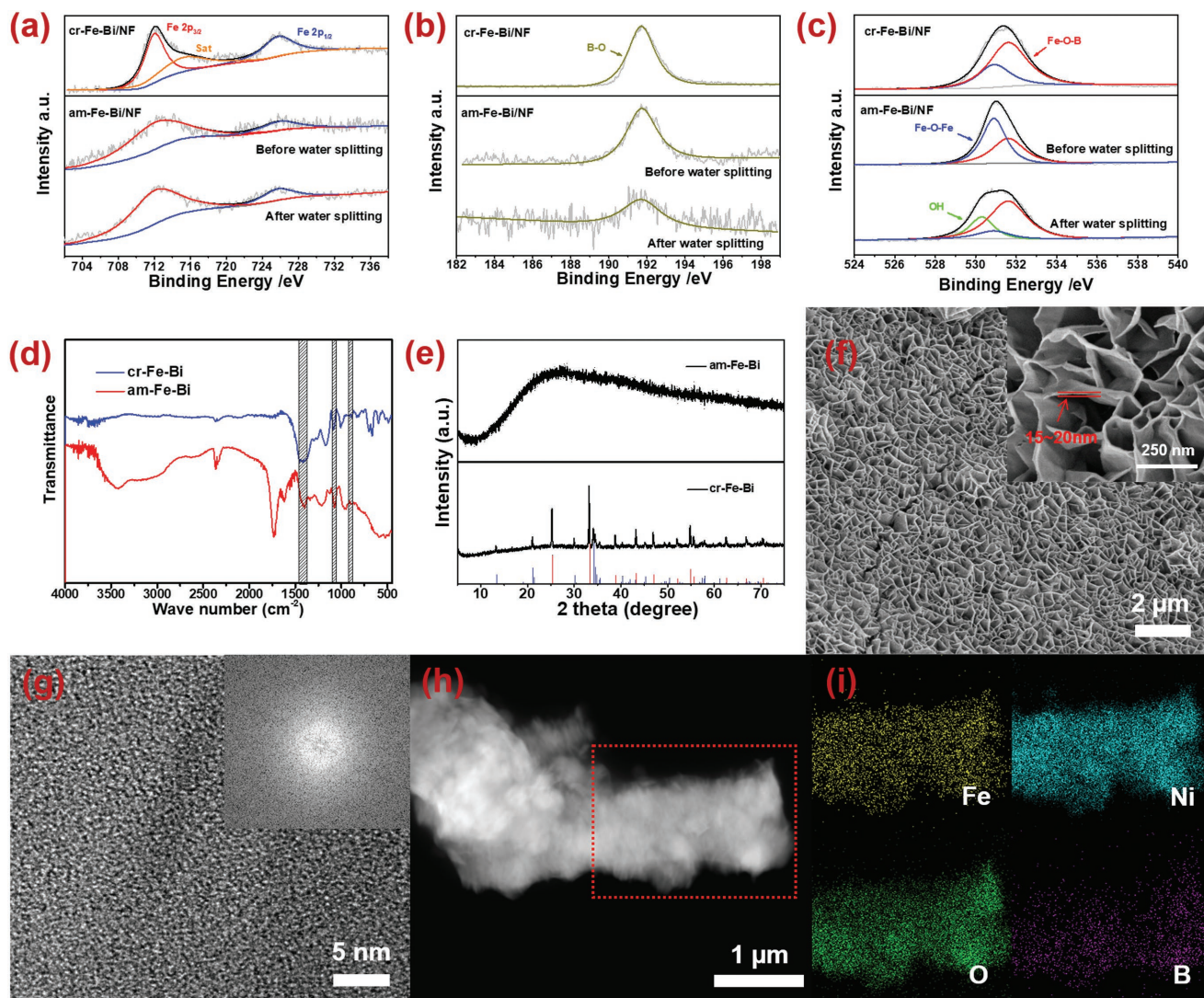


Figure 1. a–c) XPS spectra of Fe 2p, B 1s, and O 1s of cr-Fe-Bi/NF and am-Fe-Bi/NF before and after water splitting test. d) FT-IR signal of am-Fe-Bi and cr-Fe-Bi scraped from Ni foam. e) XRD signal of Fe-Bi and Fe-Bi after calcination at 650 °C (cr-Fe-Bi). f) Low-magnification SEM image of am-Fe-Bi/NF. g) HR-TEM image of am-Fe-Bi scraped from NF and inside of FFT image. h, i) The corresponding element mapping of catalysts of Fe, Ni, O, and B.

coordination interaction, which could interrupt the growth of FeOOH crystals at the solvent thermal reaction.^[29]

To investigate the electrocatalytic performance of the am-Fe-Bi/NF, the linear sweep voltammetry (LSV) was learned in 1.0 M KOH with a scan rate at 2 mV s⁻¹. Meanwhile, the control samples of bare NF, FeOOH/NF, cr-Fe-Bi/NF, and RuO₂ (same mass loading on NF through drop-coating) were also evaluated under the same condition. In **Figure 2a,c**, the am-Fe-Bi/NF showed superior OER performance with overpotentials as low as 158 and 280 mV at 10 and 300 mA cm⁻¹ current densities, respectively, which far surpass the commercial RuO₂ (228 and 300 mV at 10 and 300 mA cm⁻¹) and better than most of state-of-the-art catalysts in alkaline media (**Figure 2f**; **Table S3**, Supporting Information), while am-Fe-Bi/NF also affords overpotential at 143 mV with 10 mA cm⁻¹ current in HER, which was better than other samples except Pt/C (22 mV). In addition, the stabilities of

catalysts during HER and OER were also tested by chronoamperometric at a constant current density of 10 mA cm⁻² (**Figure 2i**), in which current density was kept stable over 30 h. However, the OER catalytic activity of FeOOH/NF (328 mV at 10 mA cm⁻¹ and 530 mV at 300 mA cm⁻¹) was poor due to the inferior electrical conductivity of crystalline FeOOH and less activity without borate.

To gain more information about the reactions kinetic, the Tafel plot during OER and HER was characterized. The lower Tafel slope of electrocatalysts indicated the higher increasing rate of electrochemical reaction with the increasing applied potential. **Figure 2b** indicates that the OER Tafel slope of am-Fe-Bi/NF was the lowest at 53 mV dec⁻¹, while the HER Tafel slope of am-Fe-Bi/NF at 75 mV dec⁻¹ is lower than that of FeOOH/NF (81 mV dec⁻¹) and cr-Fe-Bi/NF (78 mV dec⁻¹), which also approved a fast reaction kinetics (**Figure 2e**). In addition, the electrochemical impedance spectroscopy (EIS) was tested

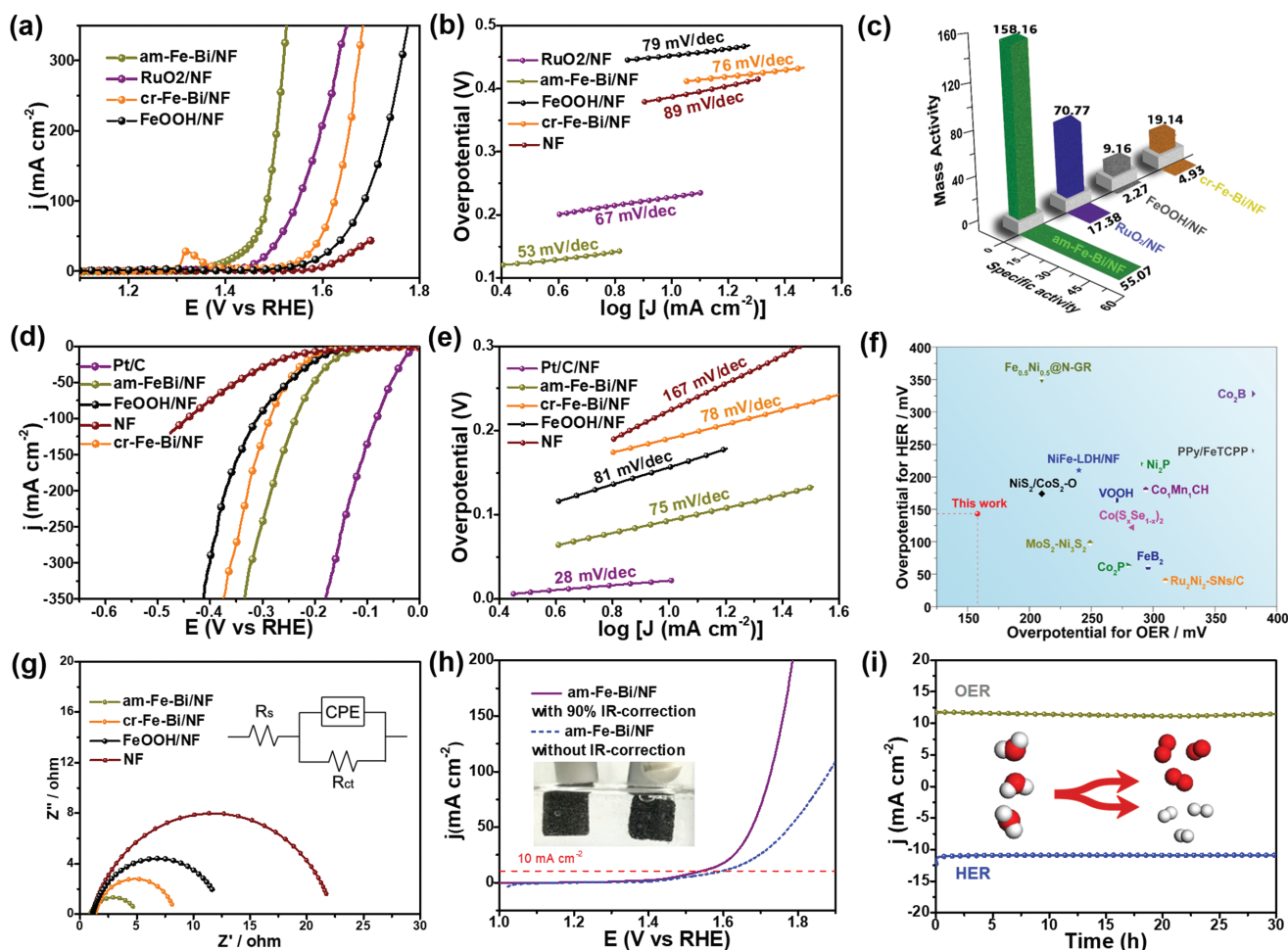


Figure 2. a) OER polarization curves for different catalysts in 1 M KOH three-electrode configuration with 90% IR-correction. b) Tafel slope of different catalysts and c) mass activity and specific activity of different catalysts calculated from electrochemical active surface area (ECSA) and current density. d,e) HER and Tafel plot performance of different catalysts in 1 M KOH three-electrode configuration with 90% IR-correction. f) Overpotential for OER and HER at 10 mA cm⁻² of state-of-the-art bifunctional electrocatalysts on 1 M KOH (Table S3, Supporting Information). g) Nyquist plots of am-Fe-Bi-NF, FeOOH/NF, and NF and the fitting curves plotted as solid traces. Inset: an equivalent circuit used for fitting data. h) Two-electrode polarization curve of am-Fe-Bi/NF//am-Fe-Bi/NF in 1 M KOH at room temperature with 90% IR-correction (purple line) and without IR-correction (blue line). i) Chronoamperometric test of OER and HER for am-Fe-Bi/NF about 30 h.

to evaluate the electrode kinetics of am-Fe-Bi/NF, FeOOH/NF, cr-Fe-Bi/NF, and different pure NF samples. Each Nyquist plot has also fitted with a simplified Randle circuit model inset. As shown in Figure 2g and Table S1 (Supporting Information), am-Fe-Bi/NF possesses much smaller R_{ct} , which demonstrated the higher conductivity.^[30] Furthermore, the mass activity and specific activity of these catalysts were calculated. As shown in Figure 2c, am-Fe-Bi/NF shows the best of catalytic active sites (mass activity: 158.16 A g⁻¹; specific activity: 55.07 mA), both of which were higher than that of RuO₂ (70.77 A g⁻¹ and 17.38 mA) and other samples (FeOOH/NF: 9.61 A g⁻¹ and 2.27 mA; cr-Fe-Bi/NF: 19.16 A g⁻¹ and 4.93 mA). The improved electrochemical performance of am-Fe-Bi/NF is ascribed to the optimized mass transfer, higher conductivity, and more catalytic active sites through introduction of borate. Besides, the synergistic effects between Fe and borate and flexible chemical bond inside amorphous structure could effectively exposed more active sites and accelerate mass transfer during reaction.

Inspired by the narrow gap between the overpotentials of OER and HER (1.53 V at 10 mA cm⁻² and 1.72 V at 100 mA cm⁻²; Figure S9, Supporting Information), an asymmetry two-electrode cell with am-Fe-Bi/NF as anode and cathode (am-Fe-Bi/NF//am-Fe-Bi/NF) was assembled to evaluate the performance of overall water splitting in 1 M KOH electrolyte. The LSV curves in Figure 2h displayed the driving voltage of 1.56 V at the current density of 10 mA cm⁻² and 1.73 V at 100 mA cm⁻² with 90% IR-correction overall water splitting cell (1.59 V at the current density of 10 mA cm⁻² and 1.86 V at 100 mA cm⁻² without IR-correction), which was the one of the best electrocatalysts in alkaline solution so far as we know (Figure 2f). Multiple chronoamperometric curve (Figure S10b, Supporting Information) also demonstrated the outstanding charge transfer capability of am-Fe-Bi/NF during the reaction. In Figure S10a (Supporting Information), the activity of overall water splitting device was kept for 30 h without obvious decay based on the chronoamperometric test. To further study the suprastability of

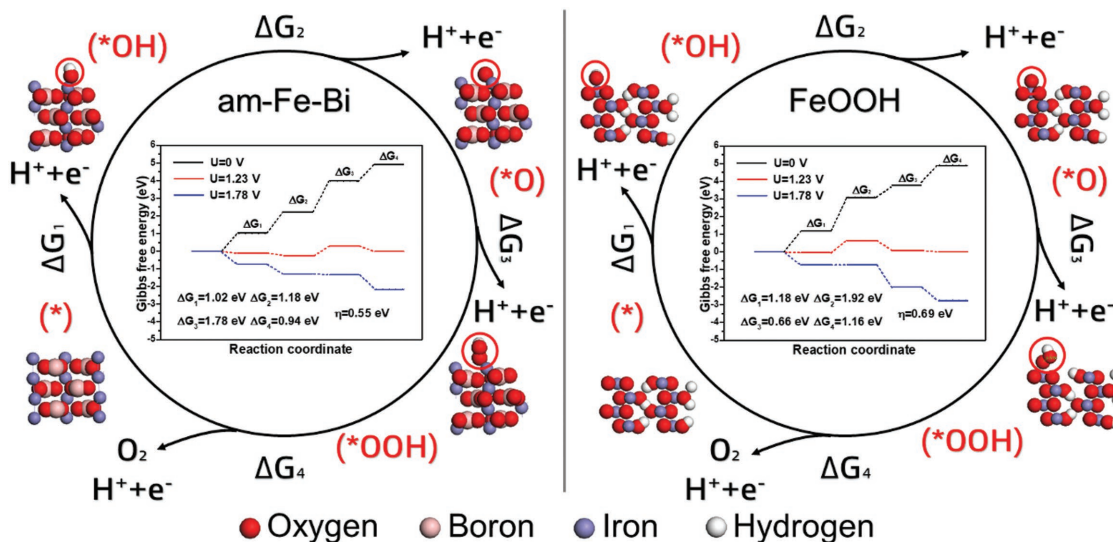
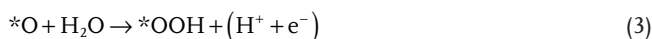
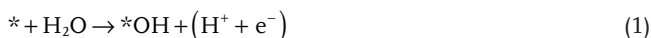


Figure 3. Gibbs free energies of Fe–Bi (left) and FeOOH (right) were calculated as follows. As shown in the figure, when $U > 1.78$ V, all steps are thermodynamically accessible for Fe–Bi and $U > 1.92$ V, all steps are thermodynamically accessible for FeOOH. The red, cyan, brown, and white atoms represent O, Fe, B, and H, respectively.

the catalyst am-Fe–Bi after reactions, the XPS, XRD, and SEM were employed on the am-Fe–Bi/NF after 30 h of water splitting. The XRD pattern (Figure S11, Supporting Information) indicated that the amorphous structure was reserved without any aggregation and crystallization. In Figure 1a–c, XPS data revealed that the binding energies of Fe 2p, B 1s are kept the same as initial, indicating the high stability of am-Fe–Bi/NF. However, the new peak of –OH in high-resolution O spectrum can be ascribed to the adsorbed hydroxyl during reaction. Moreover, the SEM image in Figure S13 (Supporting Information) supposed to the cross-link lattice morphology that still retained on the NF surface without any peel-off.

Due to the short-range order of amorphous structure and similar chemical bond between amorphous and crystal counterparts, the crystalline Fe–Bi was adopted to understand the high intrinsic activity of amorphous Fe–Bi. Gibbs free energy for each elementary reaction and d-band center (ϵ_d) were calculated. The ϵ_d was the pivotal factor in evaluating the bond strength of adsorbents on the surface of catalysts, while a relative high ϵ_d indicates the stronger absorbance.^[31] As shown in Figure S14 (Supporting Information), although the higher ϵ_d of FeOOH (–1.4816 eV) would benefit absorb reactants, it could also tightly trap the oxygen (hydrogen) hindering the release of active sites on the catalyst surface after reaction. On the contrary, the lower ϵ_d of Fe–Bi (–2.5635 eV) represents a reasonable absorption energy level, which could accelerate mass transfer through optimized balance between reactant capture capability and product releasing speed on catalytic surface.^[32] Besides, Gibbs free energy for each elementary step was calculated based on the previous work in Figure 3^[33]



Each elementary step by which the OER occurs involves adsorbed OH, O, and O intermediate products on the surface of catalysts (*). Meanwhile, to express the chemical potential at certain U , the computation hydrogen electrode was chosen and was then readily defined as $\eta = \max[\Delta G_1, \Delta G_2, \Delta G_3, \Delta G_4]/e - 1.23$ (V) which obtained from Gibbs free energy.^[34] From the standard reaction free energy of each elementary step (ΔG), as can be seen, when the electrode potential applied 0 V, all the element steps were endothermic, and the rate-determining step of model Fe–Bi was the third step to form *OOH (with $\Delta G_{* \text{OOH}} = 1.78$ eV). Different from this, the second step to form *O (with $\Delta G_{* \text{O}} = 1.92$ eV) was the rate-determining step in model FeOOH. Furthermore, the η of Fe–Bi obtained from Gibbs free energy was much lower than FeOOH/NF (0.55 V in Fe–Bi vs 0.69 V in FeOOH). Based on calculation results, the Fe–Bi possesses high intrinsic activity with less Gibbs free energy and low theoretical overpotential, which benefit the OER reaction.

As a unique trifunctional catalyst, am-Fe–Bi also possessed great electrocatalytic activity on ORR. Based on the LSV profile that tested in 0.1 M KOH, the amorphous Fe–Bi and FeOOH that scraped from NF show close onset potential to commercial Pt/C (20%), much higher than that of RuO₂ (Figure S16a, Supporting Information). The 10 h $i-t$ test also demonstrates its excellent stability (Figure S16b, Supporting Information). The better ORR performance of Fe–Bi than FeOOH would ascribe to the following reasons: 1) Fe has been widely reported as an active center for ORR; 2) changing bond length of Fe active center through introduction of borate groups would improve the performance of ORR due to Jahn–Teller distortion or back bonding. Therefore, the bond of Fe–O–B possessed rather suitable length than FeOOH which is associated with better ORR performance. Furthermore, according to the Koutechy–Levich (K–L)

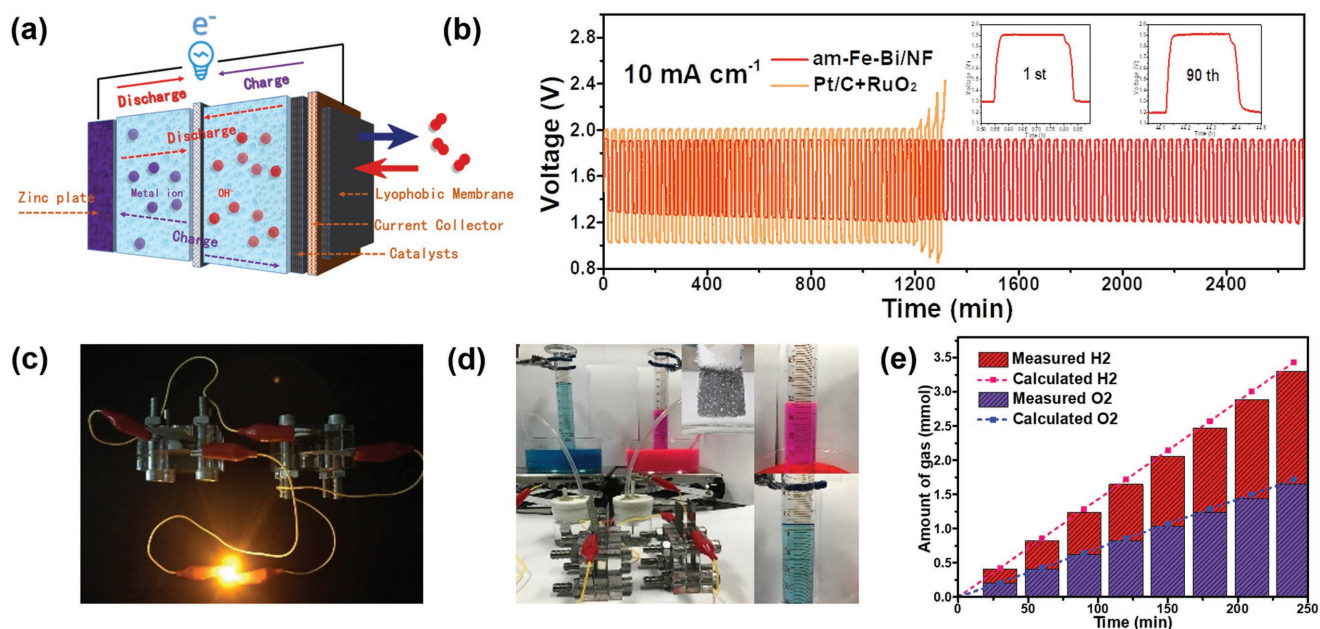


Figure 4. a) Schematic of the basic configuration of primary rechargeable zinc–air battery. b) Charging and discharging curves of different catalysts in home-made primary rechargeable zinc–air battery. c) Digital image of two-series-connected zinc–air battery powered 2.3 V LED light and d) self-driven water splitting device. e) The amount of gas theoretically calculated and experimentally measured versus time for self-driven overall water splitting of am-Fe–Bi/NF.

equation, the ORR adopts a nearly four-electron transfer process, which demonstrated superior selective and efficient reaction route (Figure S17a,b, Supporting Information). Therefore, a home-made rechargeable zinc–air battery with am-Fe–Bi/NF air cathode, polished Zn plate anode, and 6 M KOH + 0.2 M ZnOAc electrolyte was set up (Figure 4c). Initially, the open-circuit potential (OCP) of zinc–air battery was as high as 1.481 V (Figure S18, Supporting Information). The discharge polarization curve (Figure S19a, Supporting Information) of am-Fe–Bi/NF shows the maximum power density of 61.8 mW cm⁻², which is even better than commercial Pt/C (58.7 mW cm⁻²). In Figure S19b (Supporting Information), the specific capacity of zinc–air battery was tested at current densities of 10 and 100 mA cm⁻², corresponding to 782.9 and 732.0 mAh g⁻¹ (95.4% and 89.3% utilization of 820 mAh g⁻¹ Zn theoretical capacity), respectively. The inset of Figure 4c shows two zinc–air battery powered light emitting diode (LED) lights (2.5 V). Moreover, am-Fe–Bi/NF shows the better charging and discharging polarization curves than that of RuO₂ and Pt/C in rechargeable processes (Figure S20, Supporting Information). As shown in Figure 4b, the am-Fe–Bi/NF rechargeable zinc–air battery could charge for a long time at 1.9 V and discharge at 1.3 V with a current density of 10 mA cm⁻², which exhibited a high round-trip efficiency of 68.2% at initial circle and round-trip efficiency of 63.2% after 90 times circulation. As for comparison, the mixture electrode rechargeable battery with commercial Pt/C and RuO₂ (with a mass ratio of 1:3, 3 mg cm⁻²) could initially be charged at 2.0 V and discharged at 1.2 V with a round-trip efficiency of 60.0%.^[35] After 42 cycles, the activity of the battery was degraded due to the formation of platonic oxide during positive potential exposure.^[36]

Nowadays, most of the water splitting devices were relied on the external powered source. Herein, a water splitting device

driven by a two-series-connection zinc–air battery was shown in Figure 4d, whose electrodes were all composed of am-Fe–Bi/NF. As shown in Figure 4d, hydrogen and oxygen were constantly bubbled from electrode surface and collected by water displacement. After 4 h water splitting, the volume of hydrogen was 74 mL and oxygen was 37 mL, which indicated a volume ratio 2.02:1 (inset of Figure 4d). The FE of the am-Fe–Bi/NF catalyzed water splitting was calculated to be 96.3% (Figure 4e) according to the molar rate of produced gas and consumed Zn.

Based on the above characterizations and calculation, the superior performance of am-Fe–Bi/NF could be attributed to the following reasons: i) the amorphous structure possessed relatively crumby structure that was beneficial to expose more active sites and accelerate release of oxygen and hydrogen that generated during the process of OER, ORR, and HER, which are attributed to the outstanding water-splitting performance. ii) The intrinsic activity of Fe–Bi with lower d-band center could optimize balance between reactant capture capability and product releasing speed on catalytic surface, which were also demonstrated by density functional theory calculation. iii) The synergistic effects between large negative charge ion of borate and catalytic active transition metal Fe would bring multifunction into one catalyst, which also improved the durability.

In summary, the amorphous Iron borate with cross-linked nanolattices was controllably grown on Ni foam through the mild wet-chemical process. The introduction of borate plays an essential role on the formation of amorphous Fe–Bi, which could accelerate mass transfer and expose more active sites during catalyzing, while the synergistic effects between borate and Fe lead the multifunctional catalyst. As the result, the am-Fe–Bi/NF-based overall water splitting cell could be driven by 1.56 V with the current density of 10 mA cm⁻² and 1.73 V

with 100 mA cm⁻², which was the one of the best electrocatalysts in alkaline solution so far as we know. Additionally, the am-Fe-Bi/NF-based rechargeable zinc-air battery shows high OCP of 1.481 V and extremely stable cycling stability, which could regularly work more than 2600 min at the current density of 10 mA cm⁻². And particularly, the self-driven water splitting device that could be powered by two-series-connected zinc-air battery was designed to provide efficient ways about energy conversion from chemical energy to sustainable energy, in which electrodes were all composed by am-Fe-Bi/NF.

3. Experimental Section

Synthesis of am-Fe-Bi/NF, FeOOH/NF, and cr-Fe-Bi/NF: am-Fe-Bi/NF was synthesized by a simple solvent thermal method. A piece of Ni foam was washed with HCl, acetone, and ethanol three times to ensure the removal of oxidation layer. Then, 1 mmol of anhydrous ferric chloride, 0.153 g of sodium borohydride, and 0.2 g of methenamine were dissolved in 24 mL THF and 12 mL EG with continuous stirring for 2 h to make homogeneous solution. After the solution prepared, they were transferred to an 80 mL Teflon-lined autoclave and sealed with Ni foam and heated at 180 °C for 24 h. After the autoclave cooled down to room temperature, the catalysts were collected and washed with water and ethanol several times, then dried at 60 °C for 12 h in a vacuum oven. For comparison, cr-Fe-Bi-NF was synthesized by calcination of am-Fe-Bi/NF at 650 °C, and FeOOH/NF was synthesized by the same method without adding sodium borohydride at first.

Synthesis of Fe-Bi, FeOOH, and cr-Fe-Bi: Fe-Bi and FeOOH were synthesized by the same ways of am-Fe-Bi/NF and FeOOH/NF except for adding Ni foam. cr-Fe-Bi was synthesized by calcination of am-Fe-Bi at 650 °C.

Materials' Characterization: The crystalline phases of the samples were characterized by XRD using an X-ray diffractometer with Cu K α radiation. The morphologies and elemental compositions of the samples were characterized by TEM (JEM-2100UHR, Japan) equipped with an EDS. Raman spectra were measured on a Renishaw DXR Raman spectroscopy system with a 532 nm laser source. XPS (Thermo Scientific ESCALab250Xi) was used to analyze the chemical states of elements on the samples surface.

Electrochemical Measurements: Electrochemical measurements were conducted using 760E Bipotentiostat (CH Instruments) at 25 °C as a typical three-electrode system, in which am-Fe-Bi/NF was used as the working electrode, large surface area carbon rod as the counter electrode, and Hg/HgO (1 M NaOH) as the reference electrode. The HER and OER performances were recorded from the LSV polarization curves in 1 M KOH with a scan rate of 2 mV s⁻¹. The overall water-splitting system was received using am-Fe-Bi/NF as both anode and cathode in two-electrode configuration. All potential in this work was measured versus the reversible hydrogen electrode (RHE), which was converted from the following equation: $E(\text{RHE}) = E(\text{HgO}/\text{Hg}) + 0.098 + 0.059 \times \text{pH}$ with 90% IR-compensation unless specifically indicated.

Supporting Information

Supporting Information is available from the Wiley Online Library or from the author.

Acknowledgements

This work was supported by the National Natural Science Foundation of China (Grant Nos. 21572269, 51873231), and Fundamental Research Funds for Chinese Central Universities17CX05015, Key Research and

Development Program of Shandong Province, China 2017GGX40118, the Financial Support from Taishan Scholar Project.

Conflict of Interest

The authors declare no conflict of interest.

Keywords

amorphous materials, DFT calculation, overall water splitting, rechargeable zinc-air battery, self-driven

Received: July 19, 2018

Revised: August 22, 2018

Published online: September 27, 2018

- [1] G. Brumfiel, *Nature* **2003**, 422, 104.
- [2] M. K. Debe, *Nature* **2012**, 486, 43.
- [3] B. C. H. Steele, A. Heinzl, *Nature* **2001**, 414, 345.
- [4] Z. Xia, *Nat. Energy* **2016**, 1, 16155.
- [5] R. Jasinski, *Nature* **1964**, 201, 1212.
- [6] V. Dusastre, *Nature* **2001**, 414, 331.
- [7] L. Osmieri, R. Escudero-Cid, A. H. A. Monteverde Videla, P. Ocón, S. Specchia, *Appl. Catal., B* **2017**, 201, 253.
- [8] Y. Zhang, B. Ouyang, J. Xu, S. Chen, R. S. Rawat, H. J. Fan, *Adv. Energy Mater.* **2016**, 6, 1600221.
- [9] T. Tang, W. J. Jiang, S. Niu, N. Liu, H. Luo, Y. Y. Chen, S. F. Jin, F. Gao, L. J. Wan, J. S. Hu, *J. Am. Chem. Soc.* **2017**, 139, 8320.
- [10] Y. Shi, B. Zhang, *Chem. Soc. Rev.* **2016**, 45, 1529.
- [11] Y. Liang, Y. Li, H. Wang, H. Dai, *J. Am. Chem. Soc.* **2013**, 135, 2013.
- [12] M. Fang, G. Dong, R. Wei, J. C. Ho, *Adv. Energy Mater.* **2017**, 7, 1700559.
- [13] J. Yin, Y. Li, F. Lv, M. Lu, K. Sun, W. Wang, L. Wang, F. Cheng, Y. Li, P. Xi, S. Guo, *Adv. Mater.* **2017**, 29, 1704681.
- [14] D. McAteer, I. J. Godwin, Z. Ling, A. Harvey, L. He, C. S. Boland, V. Vega-Mayoral, B. Szydłowska, A. A. Rovetta, C. Backes, J. B. Boland, X. Chen, M. E. G. Lyons, J. N. Coleman, *Adv. Energy Mater.* **2018**, 8, 1702965.
- [15] Y. Guo, P. Yuan, J. Zhang, Y. Hu, I. S. Amiinu, X. Wang, J. Zhou, H. Xia, Z. Song, Q. Xu, S. Mu, *ACS Nano* **2018**, 12, 1894.
- [16] H. Huang, Y. He, Z. Lin, L. Kang, Y. Zhang, *J. Phys. Chem. C* **2013**, 117, 22986.
- [17] G. Zhu, R. Ge, F. Qu, G. Du, A. M. Asiri, Y. Yao, X. Sun, *J. Mater. Chem. A* **2017**, 5, 6388.
- [18] C. You, Y. Ji, Z. Liu, X. Xiong, X. Sun, *ACS Sustainable Chem. Eng.* **2018**, 6, 1527.
- [19] W. J. Jiang, L. Gu, L. Li, Y. Zhang, X. Zhang, L. J. Zhang, J. Q. Wang, J. S. Hu, Z. Wei, L. J. Wan, *J. Am. Chem. Soc.* **2016**, 138, 3570.
- [20] Y. Liu, J. Zhang, S. Wang, K. Wang, Z. Chen, Q. Xu, *New J. Chem.* **2014**, 38, 4045.
- [21] L. An, Y. Li, M. Luo, J. Yin, Y.-Q. Zhao, C. Xu, F. Cheng, Y. Yang, P. Xi, S. Guo, *Adv. Funct. Mater.* **2017**, 27, 1703779.
- [22] P. D. Tran, T. V. Tran, M. Orio, S. Torelli, Q. D. Truong, K. Nayuki, Y. Sasaki, S. Y. Chiam, R. Yi, I. Honma, J. Barber, V. Artero, *Nat. Mater.* **2016**, 15, 640.
- [23] W. Liu, H. Liu, L. Dang, H. Zhang, X. Wu, B. Yang, Z. Li, X. Zhang, L. Lei, S. Jin, *Adv. Funct. Mater.* **2017**, 27, 1603904.
- [24] L. Yang, Z. Guo, J. Huang, Y. Xi, R. Gao, G. Su, W. Wang, L. Cao, B. Dong, *Adv. Mater.* **2017**, 29, 1704574.

- [25] T. Tang, W.-J. Jiang, S. Niu, N. Liu, H. Luo, Q. Zhang, W. Wen, Y.-Y. Chen, L.-B. Huang, F. Gao, J.-S. Hu, *Adv. Funct. Mater.* **2018**, *28*, 1704594.
- [26] J. Zheng, X. Liping, H. Zhongyi, Q. Liang, M. Lin, C. Aixi, H. Sheng, Q. Jianwei, F. Xisheng, *PLoS One* **2014**, *9*, e83501.
- [27] W. J. Jiang, S. Niu, T. Tang, Q. H. Zhang, X. Z. Liu, Y. Zhang, Y. Y. Chen, J. H. Li, L. Gu, L. J. Wan, J. S. Hu, *Angew. Chem., Int. Ed.* **2017**, *56*, 6572.
- [28] G. S. Jia Yongzhong, X. Shuping, L. Jun, *Spectrochim. Acta, Part A* **2000**, *56*, 1291.
- [29] G. W. Schaeffer, J. S. Roscoe, A. C. Stewart, *J. Am. Chem. Soc.* **1956**, *78*, 729.
- [30] B.-A. Mei, O. Munteshari, J. Lau, B. Dunn, L. Pilon, *J. Phys. Chem. C* **2018**, *122*, 194.
- [31] J. R. Kitchin, J. K. Norskov, M. A. Barteau, J. G. Chen, *J. Phys. Chem.* **2004**, *120*, 10240.
- [32] C. Ling, L. Shi, Y. Ouyang, X. C. Zeng, J. Wang, *Nano Lett.* **2017**, *17*, 5133.
- [33] M. Bajdich, M. Garcia-Mota, A. Vojvodic, J. K. Norskov, A. T. Bell, *J. Am. Chem. Soc.* **2013**, *135*, 13521.
- [34] D. Friebe, M. W. Louie, M. Bajdich, K. E. Sanwald, Y. Cai, A. M. Wise, M. J. Cheng, D. Sokaras, T. C. Weng, R. Alonso-Mori, R. C. Davis, J. R. Bargar, J. K. Norskov, A. Nilsson, A. T. Bell, *J. Am. Chem. Soc.* **2015**, *137*, 1305.
- [35] J. Zhang, Z. Zhao, Z. Xia, L. Dai, *Nat. Nanotechnol.* **2015**, *10*, 444.
- [36] J. M. Jaksic, F. Nan, G. D. Papakonstantinou, G. A. Botton, M. M. Jaksic, *J. Phys. Chem. C* **2015**, *119*, 11267.